



# **Developing Superfast Super-Resolution Microscopy for Imaging Vesicle Movement Across Endothelial Cells**

Maroon 6

Department of Bioengineering  
Imperial College London

A Project Report Submitted in Partial Fulfilment of the

*MEng Biomedical Engineering &  
iBSc Medical Sciences with Biomedical  
Engineering  
Degrees*

**Supervisor:**

Professor. Peter Weinberg  
Department of Bioengineering  
Imperial College London  
p.weinberg@imperial.ac.uk

## Contents

1. Introduction.....	3
1.1 Atherosclerosis and its development .....	3
1.2 Vesicles, Paracellular Transport, and Their Roles in Atherosclerosis.....	4
1.3 Caveolae Structure: Function, Size (~60–70 nm) and Suspected Role in LDL Transcytosis .....	4
1.4 Current Imaging Techniques & Limitations .....	5
1.4.1 Confocal Microscopy:.....	5
1.4.2 Electron Microscopy (EM): .....	5
1.4.3 Total Internal Reflection Fluorescence (TIRF) Microscopy: .....	5
1.5 Super-resolution Microscopy Techniques & Their Limitations for Live-cell Vesicle Tracking .....	5
2. Project Aim .....	5
3. Material and Methods .....	6
3.1 Cell culture.....	6
3.1.1 Cell Culture and Substrate Coating.....	6
3.1.2 Fluorescent Labelling and Controls .....	6
3.1.3 Nuclear Staining and Imaging Preparation .....	7
3.2 Microscopy .....	7
3.3 FAST Method Development.....	7
3.3.1 Theoretical Basis.....	7
3.3.2 Image Preprocessing .....	7
3.3.3 PSF Characterisation.....	8
3.3.4 Axial Localisation & Accuracy Analysis .....	8
3.3.5 Computational Tools and Algorithms.....	8
3.4 Denoising Method Development .....	8
3.5 Method Validation .....	9
4 Results.....	9

4.1 HAEC Culture and Fluorescent Labelling .....	9
4.2 Parameter strength analysis.....	10
4.3 Denoising Optimisation .....	11
5 Discussion.....	12
5.1 Experimental Design Rationale .....	12
5.1.1 Rationale for Using HAECs.....	12
5.1.2 Substrate Selection for Imaging.....	12
5.1.3 Fluorophore Comparison and Justification .....	13
5.1.4 Integration of Fluorophore Insights into PSF Optimisation .....	14
5.2 Clarification on limitations .....	14
5.3 Denoising Optimisation .....	15
6 Conclusion .....	15
7 References.....	17
8 Appendix.....	20

# Acknowledgement

We would like to express our sincere gratitude to Professor Peter Weinberg for his insightful supervision and consistent guidance throughout the course of this project. His ability to break down complex concepts and his deep understanding of the subject matter played a pivotal role in shaping our scientific direction. We are also grateful for his generous support in covering the cost of microscope usage, which enabled critical parts of our imaging work.

We are especially thankful to Dr Peju Bolanle for his lab supervision, hands-on assistance with cell culture and imaging, and for patiently troubleshooting issues alongside us—even when time was tight. His support was invaluable, particularly during the more challenging phases of the wet-lab work.

We would also like to thank Ethan Rowland from the Weinberg lab and Emmanuella Li from the previous year's group project for their generous help in debugging the MATLAB code. Their insights and troubleshooting support were key to overcoming several early hurdles with the FAST pipeline.

We gratefully acknowledge Gaetan de Liedekerke Beaufort for allowing us to build on his MPhil thesis and FAST pipeline, which served as the foundation for this project.

We also thank Sara Meireles for generously sharing imaging data from her MSc research project (*Transport of macromolecules across endothelium and its relevance to atherosclerosis*, Imperial College London, 2022). These image stacks formed part of the dataset used in our software development and validation.

Finally, we thank the Department of Bioengineering at Imperial College London for granting us access to the microscopy facilities, without which this work would not have been possible.

# Developing Superfast Super-Resolution Microscopy for Imaging Vesicle Movement Across Endothelial Cells

Guo Yu, Hassan Al Hakeem, Jason Wang, Jerry Zhou, Linxi Li, Ruolin Zhao,

April 2025

## ABSTRACT

Building on previous advances in super-resolution microscopy for tracking LDL transport, this study refines a computational pipeline for 3D particle localisation through PSF analysis. While the core software framework remained unchanged, we addressed key technical limitations and validated the system's robustness. Human aortic endothelial cells (HAECs) were labelled with quantum dots (QDs), Tetraspeck microspheres, and DRAQ5 to optimise imaging conditions. Progress was initially limited by MATLAB version conflicts and insufficient error handling, which were resolved through code adjustments and improved software stability. The updated workflow demonstrated reproducible performance, and experimental models provided ground truth for assessing localisation accuracy across different QD concentrations. Although further optimisation was restricted by early technical challenges, the pipeline now offers improved reliability and ease of use. This work reinforces the applicability of PSF-based super-resolution imaging for investigating LDL transcytosis and provides a scalable framework for future studies of vesicular dynamics in vascular biology.

## 1. Introduction

### 1.1 Atherosclerosis and its development

Atherosclerosis is a chronic, progressive vascular disease and a leading cause of cardiovascular disease worldwide. It is very common – over the age of 40, individuals in generally good health have about a 50% chance of developing serious atherosclerosis [1]. The disease is marked by the gradual accumulation of lipids, primarily carried by low-density lipoproteins (LDL), within the arterial wall, leading to the formation of plaques that can obstruct blood flow and ultimately precipitate events such as heart attacks and strokes [2].

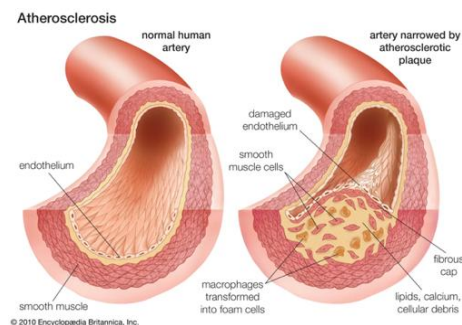


*Figure 1: A normal artery compared with an artery affected by atherosclerosis. [7]*

The development of atherosclerosis begins with endothelial dysfunction, influenced by risk factors such as hypertension, hypercholesterolaemia, diabetes, smoking and systemic inflammation. Under normal conditions, the endothelium, which consists of endothelial cells that line the inner arterial wall, acts as a selective barrier. However, when compromised, its integrity is diminished, allowing circulating LDL particles to infiltrate the subendothelial space at an accelerated rate

[3]. Once in this space, LDL is particularly vulnerable to oxidative modification, transforming it into a highly atherogenic form. Oxidised LDL exacerbates endothelial injury and triggers an inflammatory cascade wherein circulating monocytes migrate into the intima, differentiate into macrophages, and ingest oxidised LDL to become foam cells. The accumulation of foam cells forms the earliest lesion in the arteries, a fatty streak, that may evolve into complex atherosclerotic plaques [4].

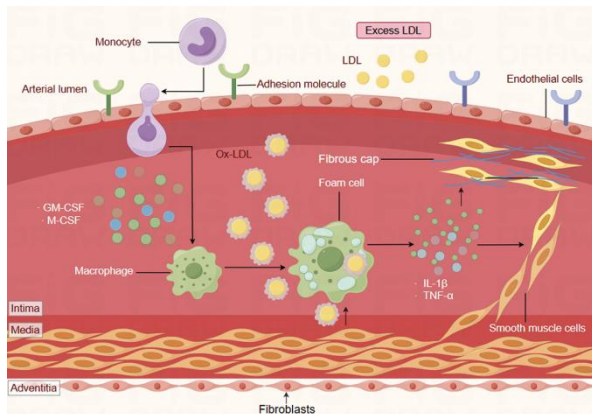


Figure 2 The pathogenesis of atherosclerosis. Designed by Figdraw ([www.figdraw.com](http://www.figdraw.com)). Colour images are available online. From paper: The Pathological Factors Involved in Current In Vitro Atherosclerotic Models[7]

As of now, there are several pharmacological therapies that reduce plasma LDL levels, such as statins, but understanding these molecular and mechanical processes is essential for developing better targeted interventions aimed at reducing LDL accumulation and mitigating the inflammatory responses that drive plaque formation [5] [6].

## 1.2 Vesicles, Paracellular Transport, and Their Roles in Atherosclerosis

Vesicles are small, membrane-bound structures involved in intracellular transport and intercellular communication. They include exosomes (30–150 nm), microvesicles, and caveolae—flask-shaped invaginations rich in cholesterol and caveolin. Exosomes form within multivesicular endosomes, microvesicles bud from the plasma membrane, and caveolae also act as signalling hubs.

Together, they transport cellular cargo and mediate the exchange of bioactive molecules.

In atherosclerosis, vesicle-mediated (transcellular) transport helps move LDL particles across endothelial cells, contributing to early lipid buildup in the arterial wall [5]. In contrast, paracellular transport allows LDL to pass between cells through tight junctions, which normally block such movement. However, inflammation, oxidative stress, or disturbed flow can disrupt these junctions, leading to passive LDL leakage [5].

Understanding whether LDL mainly crosses via vesicular or paracellular routes is key for targeted therapy. If transcytosis dominates, modulating vesicle function may help. If leakage is more important, preserving junction integrity and reducing inflammation could be more effective. Clarifying these pathways may also improve early diagnosis and guide more precise cardiovascular treatments [8].

## 1.3 Caveolae Structure: Function, Size (~60–70 nm) and Suspected Role in LDL Transcytosis

Caveolae are small, flask-shaped invaginations of the plasma membrane, typically ranging from 60 to 70 nm in diameter. They are enriched in cholesterol, sphingolipids, and caveolin-1, a structural protein essential for their formation and stability [9]. These specialised lipid rafts compartmentalise signalling molecules and receptors, facilitating processes such as endocytosis, mechano-transduction and transcytosis.

In atherosclerosis, caveolae have been implicated in the selective, transcellular transport of LDL across the endothelial barrier into the subendothelial space — a critical early event in plaque formation [10]. By investigating caveolae and the associated transport mechanisms, we can gain insights into the regulatory controls governing LDL infiltration. This understanding may open avenues for developing targeted therapies that

modulate caveolae function to inhibit early atherosclerotic events.

## **1.4 Current Imaging Techniques & Limitations**

Current imaging modalities such as confocal microscopy, electron microscopy (EM) and total internal reflection fluorescence (TIRF) microscopy have advanced our understanding of cellular structures, yet each has inherent limitations for tracking vesicles in the endothelium.

### **1.4.1 Confocal Microscopy:**

Confocal microscopy provides optical sectioning and improved contrast by rejecting out-of-focus light, benefitting live-cell imaging. However, its diffraction-limited resolution (approximately 200–300 nm) is insufficient to resolve vesicles, and its slower scanning speeds impede the tracking of rapid vesicular movements [11].

### **1.4.2 Electron Microscopy (EM):**

EM offers exceptional resolution at the nanometre scale and enables detailed visualisation of vesicles. However, the required sample preparation (fixation, dehydration and sectioning) kills the cells, making EM unsuitable for tracking dynamic, live-cell processes [12].

### **1.4.3 Total Internal Reflection Fluorescence (TIRF) Microscopy:**

TIRF microscopy delivers high signal-to-noise imaging for events near the plasma membrane (within ~100–200 nm). Despite its advantages for cell-surface events, its shallow penetration depth limits imaging of structures deeper within the cell [13][14].

In summary, while each modality contributes valuable insights, their limitations — in resolution, speed, and live-cell compatibility — highlight the need for advanced imaging

techniques for dynamic vesicular tracking in atherosclerosis.

## **1.5 Super-resolution Microscopy Techniques & Their Limitations for Live-cell Vesicle Tracking**

Super-resolution methods, including Structured Illumination Microscopy (SIM), Stochastic Optical Reconstruction Microscopy (STORM), Photoactivated Localisation Microscopy (PALM), Stimulated Emission Depletion (STED) and Points Accumulation for Imaging in Nanoscale Topography (PAINT), have extended visualisation beyond the diffraction limit. SIM enhances resolution using patterned illumination and computational reconstruction; STORM and PALM rely on stochastic fluorophore activation and localisation; STED sharpens the point spread function using a depletion laser; PAINT exploits transient fluorescent probe binding. [15]

Despite their powerful resolving capabilities, these techniques face significant challenges for live-cell vesicle tracking. Many require acquisition of multiple images over time, resulting in slow imaging speeds that cannot capture rapid vesicular dynamics effectively (sometimes taking less than a second) [16]. Furthermore, the high illumination intensities needed — especially in techniques like STED and PALM — can induce severe phototoxicity, compromising cell viability and normal cellular function [17]. In addition, the sophisticated and hardware-intensive setups increase the complexity and cost, limiting their routine use in real-time live-cell investigations [18, 19].

## **2. Project Aim**

This project develops a fast, super-resolution imaging pipeline for tracking LDL transport in endothelial cells with axial precision of about 20 nm—enough to study 60–70 nm caveolae in early atherosclerosis. We use sparse labelling to avoid PSF overlap, achieving more precise localisation than the optical

resolution limit. For axial localisation, instead of acquiring time-consuming z-stacks, we capture single optical slices and use out-of-focus PSF shape variations for accurate depth estimation. Unlike other methods relying on lens aberrations, our approach uses computational analysis of PSF features to achieve axial super-resolution without adding extra hardware. Combining sparse tagging, machine learning, and Poisson-fitted denoising, this method enables fast, high-resolution vesicle tracking that works with live-cell imaging. By providing real-time, nanoscale observation of LDL transcytosis without complex equipment, our system offers a scalable, platform-independent solution for studying vascular lipid uptake and identifying potential interventions in cardiovascular disease.

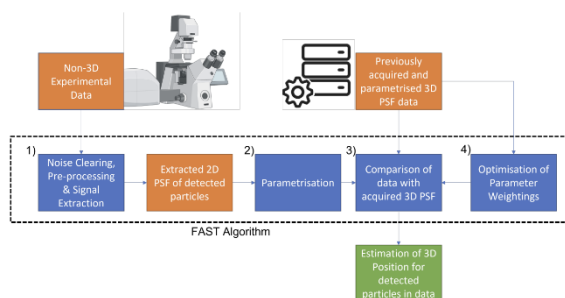


Figure 3: High Level overview of the FAST algorithm. Not shown are the registration[17]

## 3. Material and Methods

### 3.1 Cell culture

#### 3.1.1 Cell Culture and Substrate Coating

Human Aortic Endothelial Cells (HAECs) were chosen over HUVECs due to their closer representation of arterial physiology, making them a more suitable model for atherosclerosis studies. Cells were expanded from passages 3–5 and seeded onto biotinylated gelatin-coated or uncoated culture dishes (details in Appendix B). HAECs were grown to ~30–40% confluency to reduce overlap and enable clear cytoplasmic segmentation. After introducing the relevant fluorescent probes

(e.g., TetraSpeck™ microspheres, QDs), cells were fixed with 4% paraformaldehyde (PFA) for 15 minutes at room temperature, then for dedicated wells, we stained the cells' nuclei with DRAQ 5 (Appendix B).

Different dish substrates such as standard plastic, glass-bottom, or polymer-bottom were also compared for imaging performance and cell adhesion; full preparation steps and coating procedures are described in Appendix B. To evaluate the impact of gelatin coating on imaging performance and cell adhesion, both coated and uncoated wells were used in parallel. Imaging contrast and background signals were compared across conditions to assess the functional contribution of the coating.

#### 3.1.2 Fluorescent Labelling and Controls

Initial microscopy optimisation was performed using Q-dot particles. However, these were ultimately not used in the final imaging experiments. At higher magnifications, elevated background noise and fluctuating signal intensity were observed, attributed to quantum dot blinking artefacts, which compromised image stability and quantitative analysis in live-cell imaging systems.

To address this, Instead, TetraSpeck™ Fluorescent Microspheres (100 nm; Invitrogen, T7279) were adopted as fiducial markers for PSF calibration and algorithm validation (Appendix B). Their multi-channel emission (365/430 nm, 505/515 nm, 560/580 nm, and 660/680 nm) and high photostability offered stable reference points in the presence of real cellular structures. Additionally, FITC-conjugated avidin was employed as a control to evaluate biotin–avidin specificity and detect possible background signal sources. Detailed preparation and fixation protocols can be found in Appendix B.

As an additional control, FITC-conjugated avidin (BD Biosciences, 554057) was used to



assess the specificity and uniformity of biotin-avidin binding and to identify potential sources of background signal arising from incomplete surface blocking.

### **3.1.3 Nuclear Staining and Imaging Preparation**

To facilitate nuclear segmentation and assess cellular morphology during imaging, nuclei were labelled with DRAQ5™, a cell-permeable dye that is compatible with both live and fixed cells, making it suitable for real-time microscopy without compromising cell viability. We were able to use the labelled nuclei to find the correct z-plane on which other labels could be imaged. The far-red emission spectrum of DRAQ5™ (excitation/emission maxima: 646/697 nm) ensured minimal spectral overlap with green fluorophores (e.g. FITC, Alexa Fluor 488) used elsewhere in the study, enabling multiplexed imaging of nuclear and vesicular signals with minimal crosstalk, but not with QDs.

Following fixation, cells were incubated with DRAQ5™ at a final concentration of 2  $\mu$ L in complete growth medium for 5 minutes at 37 °C. Stained samples were then imaged using confocal microscopy.

## **3.2 Microscopy**

After preparing the different models, a Leica SP8 Confocal Microscope was used to visualise QDot 800, FITC-avidin, and TetraSpeck™ microspheres across various concentrations. Image acquisition included both fluorescence and brightfield modes at 10 $\times$  and 20 $\times$  magnification using an air objective. Excitation and emission settings were adjusted to match each marker's spectral properties. Single optical slices were captured to evaluate marker intensity, spatial distribution, and compatibility with subsequent analyses.

## **3.3 FAST Method Development**

### **3.3.1 Theoretical Basis**

The FAST (Fast Axial Super-Resolution Technique) method is built on two main ideas: sparse tagging and PSF-based axial localization. Sparse tagging reduces fluorophore density to prevent signal overlap, allowing easier detection of individual particles and improving localization accuracy.

Instead of relying on specialized optics, FAST uses natural changes in PSF shape as particles shift along the Z-axis. This is achieved by scanning immobilized fluorescent particles at different depths under consistent imaging conditions to build a 3D PSF reference dataset. During imaging, single-frame PSFs are matched against this reference, and axial positions are estimated using a combination of a genetic algorithm and linear regression [20][21]. This removes the need for layer-by-layer scanning and significantly speeds up the process.

### **3.3.2 Image Preprocessing**

Image preprocessing helps reduce noise and isolate reliable PSF signals. It starts with background subtraction using the Iterative Least-Squares Difference (ILD) method, followed by Poisson-Gaussian noise modelling [22]. In some cases, wavelet filtering is also used to improve signal-to-noise ratio [23][24].

After denoising, thresholding is applied to retain only bright regions likely to contain particles. Depending on image properties, either global or adaptive thresholding is used. These regions are converted into binary images and segmented using connected component analysis. Morphological operations are then applied to remove artefacts before extracting the final ROIs.

Detected objects are filtered based on size and shape [25]. To improve accuracy, each candidate is compared to a Gaussian PSF template using Spearman's rank correlation

[25]. Valid ROIs are selected, and Gaussian masks are fitted to their centres to refine localisation.

### 3.3.3 PSF Characterisation

To create a reference, fluorescent particles are scanned along the Z-axis under consistent imaging conditions. The resulting z-stacks are processed using the same pipeline as experimental images. As particles move out of focus, their PSFs become wider and dimmer. This predictable shape change allows axial position to be estimated from a single 2D image.

Each PSF is described by a feature vector capturing shape properties such as roundness, symmetry, directional distortion, and deviation from a Gaussian profile. Many of these features are adapted from computer vision and selected for their robustness to noise [25]. The feature vectors are then mapped to known Z-positions using regression, allowing new PSFs to be localized without further scanning.

### 3.3.4 Axial Localisation & Accuracy Analysis

Axial localization is performed by feeding PSF feature vectors into a regression model trained to predict Z-positions. Since PSF shape changes predictably with defocus, depth can be estimated from a single image without scanning.

To improve accuracy, a genetic algorithm tunes feature weights over 200 generations by minimizing RMSE [20][26]. With each cycle of mutation, crossover and selection, the model becomes more precise.

To resolve the symmetry ambiguity near the focal plane, a random forest classifier is added [25]. It learns to detect subtle asymmetries in PSFs that indicate whether a particle is above or below focus. This combined approach was

tested on bead and LDL datasets, reaching axial localization accuracy of 14–20 nm without scanning or specialized optics.

### 3.3.5 Computational Tools and Algorithms

The FAST method was implemented in MATLAB using custom scripts for tasks like background subtraction, PSF segmentation, and ROI extraction. The feature extraction process was designed modularly, making it easier to test and combine different descriptors based on the application.

The full pipeline supports batch processing and allows parameters to be adjusted through config files. Results, including localization data and feature vectors, are saved in structured formats for further analysis in MATLAB or FIJI.

## 3.4 Denoising Method Development

Building on the framework developed by last year's 4082 group project and drawing insights from the MPhil thesis of de Liedekerke Beaufort [27], and considering the limitations mentioned in their filtering models, we developed a new adaptive wavelet-based filtering approach (see Appendix D). The stack is first decomposed using discrete wavelet transform (DWT) with the 'sym4' wavelet basis. For each slice in the stack, a universal threshold is calculated using Donoho's universal threshold formula [28]:

$$T = \frac{\text{median}(|C_i|)}{0.6745} \times \sqrt{2 \log(N)}$$

where  $C$  denotes the wavelet detail coefficients and  $N$  is the total number of pixels. And then soft thresholding is applied to the wavelet coefficients [28]:

$$C_i^{\text{soft}} = \begin{cases} C_i - T, & \text{if } C_i > T \\ C_i + T, & \text{if } C_i < -T \\ 0, & \text{if } |C_i| \leq T \end{cases}$$

soft thresholding removes weak coefficients (typically noise) and shrinks strong ones to reduce signal bias, helping preserve meaningful features while suppressing noise and smoothing the reconstruction. After reconstructing the image from the thresholded coefficients using inverse DWT, an additional adaptive background threshold is applied to remove low-intensity background fluorescence. This threshold is defined as [29]:

$$T_{back} = \lambda + 0.5\sigma$$

where  $\lambda$  and  $\sigma$  represent the mean and standard deviation of the background, respectively. This allows weak background signals to be filtered out while retaining meaningful features.

### 3.5 Method Validation

To validate the FAST algorithm, TetraSpeck™ fluorescent microspheres (100 nm) and quantum dots (~20 nm) were immobilised in gelatin-coated glass-bottom wells and imaged using the Leica SP8 confocal microscope. Z-stacks were acquired at 50–100 nm intervals to generate reference axial positions across the focal depth. Particles were registered across frames, and their focal planes were determined using gradient-based focus metrics. These ground truth positions were used to evaluate FAST-derived localisations from single-plane widefield images.

Comparative validation was also conducted using existing datasets from the 2023 group project and the MPhil thesis by Gaetan de Liedekerke Beaufort. Lateral localisation was estimated via Gaussian and gradient-based centroid fitting. Axial accuracy was assessed by calculating the root mean square error (RMSE) between FAST predictions and known z-positions. Repeatability was quantified as the standard deviation of localisations at fixed depths, while detection efficiency was measured by comparing FAST outputs against known particle positions in the z-stacks.

## 4 Results

### 4.1 HAEC Culture and Fluorescent Labelling

HAECs were successfully cultured and maintained under standard laboratory conditions (see appendix B). The clear, consistent cell morphology, minimal debris, absence of irregularities, and full confluency indicated that the cells remained healthy, viable, and uncontaminated throughout the experiment. The robustness and reproducibility of the culturing protocol was also confirmed with the outcome. Following fixation with PFA, DRAQ5 staining clearly marked the nuclei. This provides a clear reference plane that significantly improved the ease and accuracy of locating other fluorescent markers (i.e., QDs or microspheres).

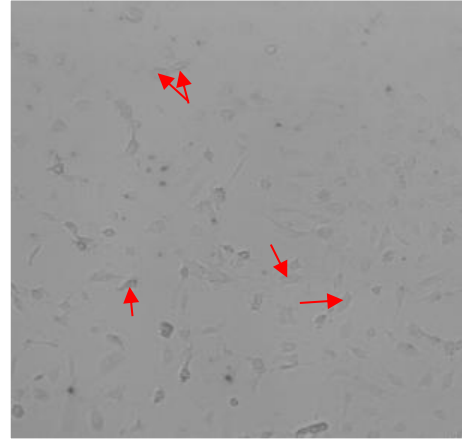


Figure 4: The Graph of HAECs in grey scale (almost all the darker patterns were HAECs)

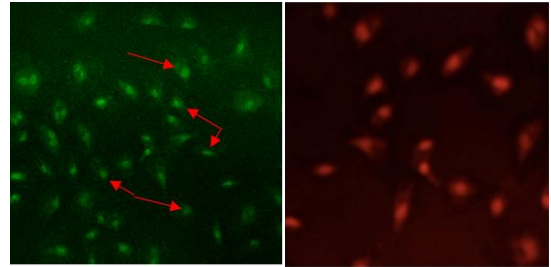


Figure 5: The Graph of DRAQ-5 stained HAECs laser channels (all of the bright spots are HAECs)

Quantum dots were successfully visualized under different laser channels alongside DRAQ-5 stained HAECs. In the composite image, the high density of QDs on the gelatin layer creates a visual effect reminiscent of a

layer of golden dust (each single pixel is a Q-dot), while the HAEC nuclei, labelled with DRAQ-5, appear distinctly under the red laser channel. However, due to a slight overlap in the emission wavelengths of QDs and DRAQ-5, the combined-channel image exhibited increased noise but still easy to be visualized.

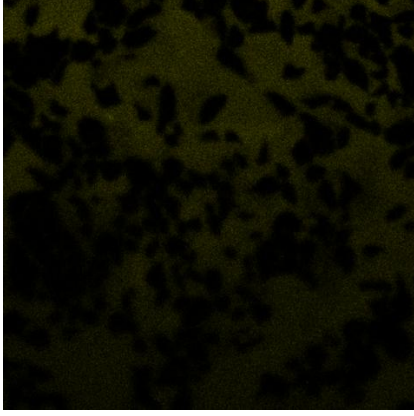


Figure 6: The Graph of Quantum dots with DRAQ-5 stained HAECs under yellow laser channel (all of the yellow pixels were quantum dots and black patterns were HAECs nuclei)

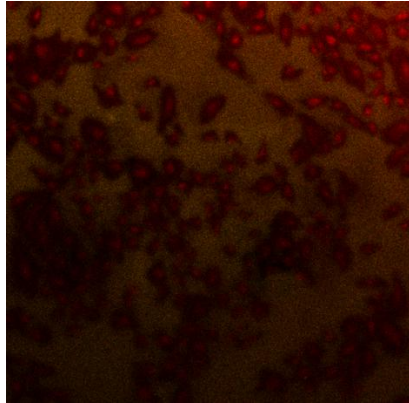


Figure 7: The Graph of Quantum dots with DRAQ-5 stained HAECs under yellow and red laser channels (noise because of wavelength overlapping)

## 4.2 Parameter strength analysis

To evaluate the how the strength and sensitivity of each parameter varies with axial position, a representative set of 20 representative PSF stacks was processed. These stacks were generated using data acquired by Sara Meireles during her MSc research project at Imperial College London in 2022 [30]. Each PSF stack consists of a centred fluorescent marker scanned at 80nm axial intervals, ranging from -400nm to 400nm relative to the focal plane of the objective lens - with negative values indicating positions below the focal plane

(towards the coverslip) and positive values indicating positions above it (deeper into the sample). This allows us to link calculated parameter values with depth, giving us an indication of the responsiveness of the parameters to change in axial location.

A total of 33 parameters were investigated (see Appendix C for definition of all 33 parameters), while many exhibited only little variations with depth (almost flat) such as M8 (the 8<sup>th</sup> parameter) and M10 in Figure.8, several parameters (M7, M9, M23, M24) stood out, demonstrating a pronounced consistent trend across the scanned depth range.

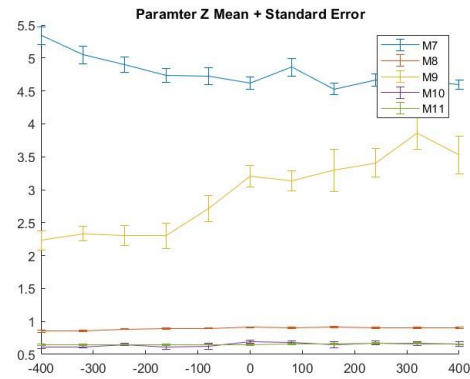


Figure 8 shows the parameter mean and standard error of parameter 7 to 11. While others are mostly flat, M7 and M9 shows stronger consistent change across scanned depths.

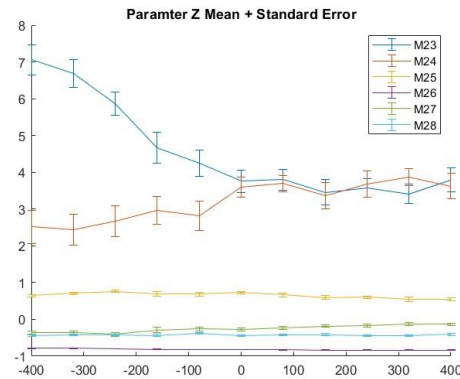


Figure 9 shows the parameter mean and standard error of parameter 23 to 28. M23 and M24 shows stronger consistent change across scanned depths.

$M_9$	$M_9 = Med(I - Med(I))$
$M_{23}$	$M_{23} = \frac{\sum_{n=1}^N \left( \sqrt{x_{gauss,n}^2 + y_{gauss,n}^2} \right)}{E(I) \sum_{n=1}^N I_n}$

Table 1 shows the mathematical equation for calculating  $M_9$  and  $M_{23}$

Two of the most responsive parameters were  $M_9$ , a robust measure of spread in pixel intensities around the median, and  $M_{23}$ , a distance-based metric reflecting how broadly the PSF extends from its centre after weighting by intensity. Both parameters have shown steeper change with change in axial location while having acceptable standard error, making them strong indicators for depth estimation.

By identifying varying strengths of axial location predictors, we can guide the genetic algorithm to emphasise on stronger parameters within its evolving coefficients set. In effect, the GA should converge more rapidly and reliably by assigning larger weightings to more responsive parameters such as  $M_9$  and  $M_{23}$ .

### 4.3 Denoising Optimisation

To compare the denoising methods, we applied the fitted noise model, Samuel's wavelet method, and our adaptive wavelet filter to the same input image. Due to confocal microscope scheduling issues, we couldn't obtain the final stack, so we used Sarah's stacks 1 to 10 instead.

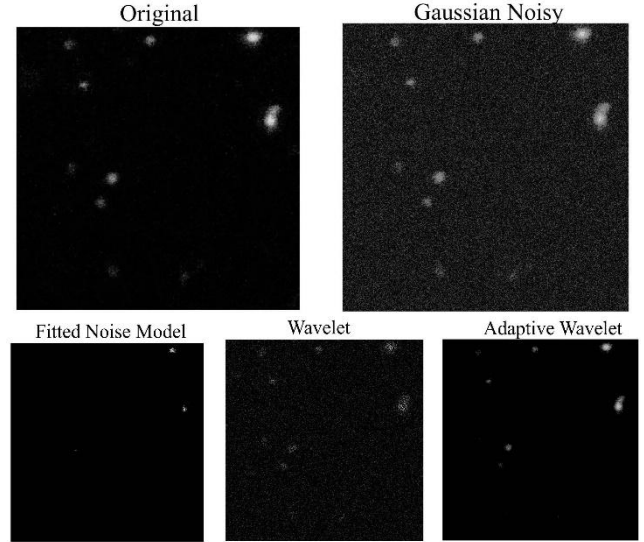


Figure 10 Graphs of original stack and Gaussian noisy stack and graphs after filtered by 3 different filters respectively

As shown in Figure 10, the three methods differ in background suppression and signal retention. The fitted model gives a clean output but with sparse signals and rough edges. Samuel's wavelet preserves more features but introduces more noise. In contrast, our adaptive wavelet retains finer details with less background interference.

Model	MSE	PSNR/dB	SSIM
Fitted Noise	0.0020	27.04	0.6260
Wavelet	0.0027	25.64	0.3964
Adaptive Wavelet	0.0006	32.57	0.6327

Table 2 shows MSE, PSNR and SSIM of 3 different filters

We also performed a quantitative evaluation of the results using Mean Squared Error (MSE), Peak Signal-to-Noise Ratio (PSNR), and Structural Similarity Index (SSIM). As shown in Table 2, the adaptive wavelet method achieved the lowest MSE and the highest SSIM and PSNR among the three methods, indicating superior signal fidelity and structural preservation.



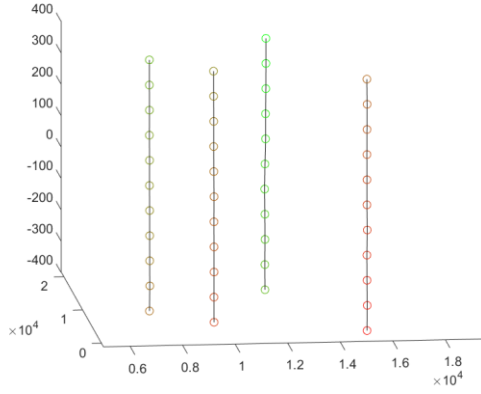


Figure 11 z-localization of PSFs mapped to known z-stack depths after denoising with the fitted model. Four PSFs were obtained.

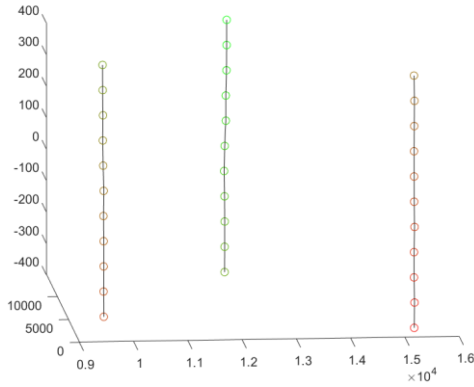


Figure 12 z-localization of PSFs mapped to known z-stack depths after denoising with the adaptive wavelet filter. Only three PSFs were retained due to stricter filtering.

Finally, we evaluated PSF localization along the z-axis using both the fitted noise model and our adaptive wavelet method. As shown in Figure 11, the fitted model retained four PSFs, while Figure 12 shows only three for the adaptive method.

This is because our approach filtered out one PSF that didn't meet the shape or consistency criteria, using a two-step process. First, wavelet soft thresholding suppresses weak coefficients, typically noise, in the transform domain. Then, after reconstruction, a background threshold removes low-intensity signals near the noise floor.

By keeping only well-defined PSFs, our method may offer more accurate depth localization. This selective filtering reduces

the chance of including unstable PSFs, improving the overall reliability of axial localization.

## 5 Discussion

### 5.1 Experimental Design Rationale

#### 5.1.1 Rationale for Using HAECs

Human Aortic Endothelial Cells (HAECs) were chosen over Human Umbilical Vein Endothelial Cells (HUVECs) to better replicate the haemodynamic and structural conditions where atherosclerosis typically begins. The aorta, a common site of early plaque formation, is exposed to pulsatile flow and high pressure, both of which influence endothelial behaviour [31][32]. While HUVECs are commonly used due to their accessibility, their venous origin limits their relevance in arterial disease models. This is highlighted by the failure of venous grafts in arterial bypass surgeries, where sustained arterial pressure causes maladaptive remodelling, wall thickening, and re-occlusion [33][34][35]. In contrast, HAECs better mimic the high-pressure arterial conditions and are more suited for studying vesicular trafficking in atherosclerosis-prone regions [36].

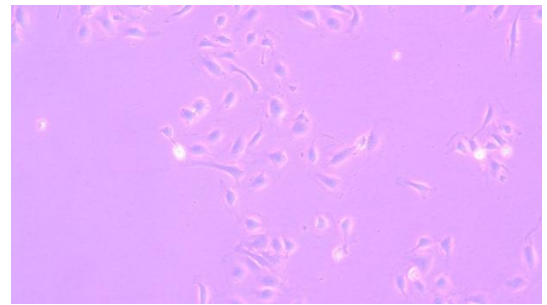


Figure 13: Human Aortic Endothelial Cells (HAECs)

#### 5.1.2 Substrate Selection for Imaging

For routine cell expansion, we used standard plastic-bottom culture plates, as previous work from Prof. Weinberg's group showed that porcine aortic endothelial cells (PAECs) adhered well to uncoated plastic without

gelatin coating [37]. Given HAECs' similar origin and adhesion properties, they also formed stable, confluent monolayers under the same conditions in pilot trials.

However, plastic substrates were unsuitable for high-resolution imaging of fluorescent markers like TetraSpeck™ microspheres and Quantum Dots (Q-dots). At 10× magnification, optical distortion and poor axial resolution prevented the software from distinguishing closely spaced PSFs. To solve this, we switched to Ibidi #1.5H glass-bottom and polymer-bottom dishes, designed for high-numerical aperture objectives with optical-grade thickness (170 µm) and a refractive index (~1.52) compatible with the Leica SP8 system [38][39].

Glass-bottom dishes were chosen for calibration due to their low autofluorescence and clarity, while polymer-bottom dishes provided more physiologically relevant stiffness for cell behaviour studies, without compromising optical performance.

For future live-cell experiments, polymer-bottom dishes will be preferred to maintain both cell morphology and imaging clarity under dynamic conditions. This is crucial for tracking vesicle motion without introducing mechanical stress or signal distortion, issues previously observed with glass-based cultures.

### **5.1.3 Fluorophore Comparison and Justification**

#### **Quantum Dots: Vesicle-Sized Surrogates for System Optimisation**

Quantum dots (QDs) were selected for their size (~20 nm), which closely mimics low-density lipoprotein (LDL) particles (22–29 nm) [40], making them valuable as experimental surrogates in transcytosis studies. Their high quantum yield and photostability support prolonged imaging, sparse labelling, and consistent axial PSF distortion — essential for FAST pipeline calibration. However, their performance was inconsistent. Fluorescence

loss occurred in some wells overnight despite identical conditions, possibly due to aggregation or degradation. Additionally, blinking behaviour [41] reduced signal stability, and spectral overlap with DRAQ5 required non-standard pinhole and gain settings, elevating background noise. These issues highlighted their sensitivity to imaging conditions and the need for better compatibility with multiplexed markers.

#### **TetraSpeck™ Microspheres: Gold Standard for Calibration**

TetraSpeck™ fluorescent microspheres (~100 nm) were used primarily for axial calibration and algorithm training. Their multi-channel emission and high photostability made them ideal for establishing a consistent PSF reference dataset. Unlike QDs, they showed no blinking and retained signal intensity across time points, enabling reproducible z-stacks for parameter analysis. Their large size precludes use as LDL analogues but made them the most reliable tool for denoising assessment and regression model development.

#### **FITC-Avidin: Low-Cost Control for Surface Specificity**

FITC-conjugated avidin (~5–7 nm) was included as a control to assess the integrity of the biotinylated gelatin substrate and measure nonspecific background signal. Its emission spectrum avoided overlap with QDs and DRAQ5, simplifying multiplexed imaging. However, due to its small size and lack of particulate structure, FITC-avidin produced diffuse signals that were difficult to treat as discrete PSFs. It was therefore unsuitable for precise localisation tasks but remained effective for troubleshooting coating consistency and baseline fluorescence levels.

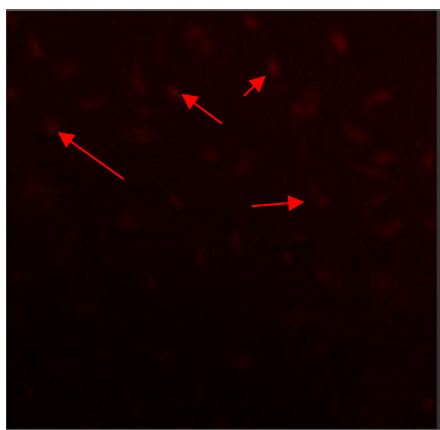


*Figure 14 Graphs of FITC- Avidin with DRAQ-5 stained cells under red channel*

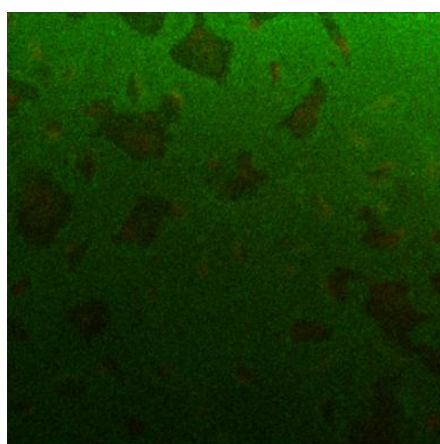


*Figure 15 Graphs of FITC-Avidin with DRAQ-5 stained cells under red and green channel*

The comparative imaging of QDs and TetraSpecks at 1:100 and 1:1000 dilutions will be completed post-submission. This will allow us to determine optimal particle concentration for sparse labelling, ensuring PSF separation and reducing overlap during live-cell imaging. Establishing these conditions is critical for maintaining the precision of localisation algorithms under biologically relevant densities.

#### **5.1.4 Integration of Fluorophore Insights into PSF Optimisation**

Using quantum dots, TetraSpeck™ microspheres, and FITC-avidin in tandem allowed us to interrogate the FAST pipeline under varied signal conditions. Each fluorophore exposed specific challenges — QDs revealed limitations in signal stability and spectral overlap, prompting stricter denoising filters. TetraSpecks offered

consistent, high-fidelity PSFs ideal for axial calibration and parameter tuning. FITC-avidin, while unsuitable for precise localisation, helped detect substrate artefacts and assess baseline noise.

This multi-fluorophore approach enhanced both the imaging protocol and signal processing pipeline, ensuring that our localisation models were tested across realistic noise profiles and biological variability. The next step will be to apply the FAST pipeline to fluorescently labelled LDL particles in fixed HAECs. This is necessary to validate whether the system can resolve particles of true biological interest under realistic signal and size conditions. Success in this phase will provide the confidence and calibration required for live-cell imaging of LDL transcytosis, which remains a key gap in atherosclerosis research.

## **5.2 Clarification on limitations**

Although the experimental setup was clear, practical constraints limited the imaging data we could collect. Sample preparation for confocal microscopy took several days, but access to the Leica SP8 system was restricted due to high demand and scheduling conflicts. This bottleneck reduced imaging opportunities and limited the range of conditions we could test.

Early in the project, limited familiarity with the confocal system also delayed data collection—especially when identifying QD-labelled particles and managing background signal. Although we became more proficient over time, the steep learning curve overlapped with key imaging periods. As a result, some control groups and comparisons were deprioritised in favour of capturing essential marker data.

A key experiment comparing Quantum Dots and TetraSpeck™ microspheres at 1:100 and 1:1000 dilutions was postponed due to microscope availability. This will be carried out after submission to assess signal stability, brightness, and PSF consistency across



fluorophore types and concentrations, particularly to address signal overlap at high labelling densities, which impairs localisation accuracy.

These challenges underscore the need for early training, proactive equipment booking, and backup plans in data-heavy workflows. Despite these issues, we obtained enough images to validate core parts of the FAST pipeline, with legacy datasets helping fill some calibration and denoising gaps.

### 5.3 Denoising Optimisation

Our adaptive wavelet method effectively removes high-frequency noise through wavelet decomposition and enhances image quality using a threshold based on background intensity. In comparison, de Liedekerke Beaufort’s fitted noise model relies on a fixed, empirically chosen threshold applied uniformly across the entire image. While this approach can reduce noise, it may also remove meaningful details, especially in cases where the background is uneven, or the signal is weak.

Samuel Mathew’s wavelet method retains signal well, but its thresholding is based on empirical adjustments, leading to higher errors and more background noise. In our exploration, we found that Stationary Wavelet Transform (SWT) performed slightly better than DWT in denoising. However, SWT requires additional MATLAB toolboxes, causing compatibility issues. Considering efficiency and complexity, we chose Discrete Wavelet

Transform (DWT), which is computationally lighter and sufficiently accurate for PSF analysis.

While testing, we noticed that de Liedekerke Beaufort’s original implementation didn’t handle extreme object sizes. When detected PSFs were either too small or abnormally

large, the script would crash. To fix this, we added a size threshold to skip problematic regions and allow the program to continue running. This improved stability and prevented the pipeline from being interrupted by invalid PSFs.

Looking ahead, further filter adjustments are planned for live-cell imaging, where background variability and PSF distortion are more dynamic. A more adaptive noise model will help retain signals without overfitting, ensuring efficient real-time processing and reliable localisation in complex conditions.

## 6 Conclusion

In conclusion, this project successfully developed the FAST pipeline for high-speed, high-precision 3D localisation of sub-resolution particles. By resolving software issues, improving stability, and validating the workflow, we established a reproducible framework for PSF-based super-resolution microscopy. Key optimisations, such as adaptive wavelet denoising and parameter analysis, improved noise suppression while preserving PSF details, enhancing downstream accuracy and efficiency. The use of Quantum Dots and Tetraspeck microspheres provided strong validation for cell-based protocols.

Despite the progress, several challenges remain. First, the workflow currently relies on fixed-cell models, so integrating real-time tracking for moving vesicles is a key next step. Second, dataset limitations due to microscopy and wet lab constraints suggest that expanding the dataset could enhance pipeline generalisability and genetic algorithm training. Finally, although this project did not optimise downstream machine learning, we identified areas for improvement in the GA and parameter selection, which could improve axial prediction robustness. In summary, these optimisations advance low-cost, minimal-hardware super-resolution imaging. By combining sparse labelling with out-of-focus PSF analysis, we offer a scalable, platform-agnostic method for capturing vesicular

processes. This pipeline has the potential to accelerate research into LDL transcytosis and broaden applications in biomedical particle tracking.

## 7 References

1. World Health Organization (2021). Cardiovascular Diseases (CVDs). [online] World Health Organization. Available at: [https://www.who.int/news-room/fact-sheets/detail/cardiovascular-diseases-\(cvds\)](https://www.who.int/news-room/fact-sheets/detail/cardiovascular-diseases-(cvds)).
2. Libby, P., Okamoto, Y., Rocha, V.Z. and Folco, E. (2010). Inflammation in Atherosclerosis: *Circulation Journal*, 74(2), pp.213–220. doi:<https://doi.org/10.1253/circj.cj-09-0706>.
3. Atherosclerosis—An inflammatory disease. (1999). *Journal of Cardiothoracic and Vascular Anesthesia*, 13(4), p.502. doi:[https://doi.org/10.1016/s1053-0770\(99\)90233-1](https://doi.org/10.1016/s1053-0770(99)90233-1).
4. Zhang, X., Sessa, W.C. and Fernández-Hernando, C. (2018). Endothelial Transcytosis of Lipoproteins in Atherosclerosis. *Frontiers in Cardiovascular Medicine*, 5. doi:<https://doi.org/10.3389/fcvm.2018.00130>.
5. American Heart Association (2024). Atherosclerosis. [online] [www.heart.org](http://www.heart.org). Available at: <https://www.heart.org/en/health-topics/cholesterol/about-cholesterol/atherosclerosis>.
6. NICE (2023). Recommendations | Cardiovascular disease: risk assessment and reduction, including lipid modification | Guidance | NICE. [online] [www.nice.org.uk](http://www.nice.org.uk). Available at: <https://www.nice.org.uk/guidance/ng238/chapter/Recommendations#statins-for-primary-prevention-of-cardiovascular-disease>.
7. Britannica (2019). Atherosclerosis | pathology. In: *Encyclopædia Britannica*. [online] Available at: <https://www.britannica.com/science/atherosclerosis>.
8. Cunningham, K., Gotlieb, A. The role of shear stress in the pathogenesis of atherosclerosis. *Lab Invest* 85, 9–23 (2005). doi:<https://doi.org/10.1038/labinvest.3700215>
9. Frank, P.G., Pavlides, S. and Lisanti, M.P. (2008). Caveolae and transcytosis in endothelial cells: role in atherosclerosis. *Cell and Tissue Research*, 335(1), pp.41–47. doi:<https://doi.org/10.1007/s00441-008-0659-8>.
10. Felix Jansen, Georg Nickenig, Nikos Werner Extracellular Vesicles in Cardiovascular Disease: Potential Applications in Diagnosis, Prognosis, and Epidemiology(2017) <https://doi.org/10.1161/CIRCRESAHA.117.310752>
11. Turkowyd, B., Balinovic, A., Virant, D., Carnero, H.G.G., Caldana, F., Endesfelder, M., Bourgeois, D. and Endesfelder, U. (2017). A General Mechanism of Photoconversion of Green-to-Red Fluorescent Proteins Based on Blue and Infrared Light Reduces Phototoxicity in Live-Cell Single-Molecule Imaging. *Angewandte Chemie International Edition*, 56(38), pp.11634–11639. doi:<https://doi.org/10.1002/anie.201702870>.
12. Hell, S.W. (2007). Far-Field Optical Nanoscopy. *Science*, 316(5828), pp.1153–1158. doi:<https://doi.org/10.1126/science.1137395>.
13. Denham, S. and Cutchey, D. (2009). Total Internal Reflection Fluorescence (TIRF) Microscopy. *Imaging & Microscopy*, 11(2), pp.54–55. doi:<https://doi.org/10.1002/imic.200990043>.
14. Trache, A. and Meininger, G.A. (2008). Total Internal Reflection Fluorescence (TIRF) Microscopy. *Current Protocols in Microbiology*, 10(1). doi:<https://doi.org/10.1002/9780471729259.mc02a02s10>.
15. Valli, J., Garcia-Burgos, A., Rooney, L.M., Oliveira, B.V. de M. e, Duncan, R.R. and Rickman, C. (2021). Seeing beyond the limit: A guide to choosing the right super-resolution microscopy technique. *Journal of Biological Chemistry*, [online] 297(1). doi:<https://doi.org/10.1016/j.jbc.2021.100791>.
16. Darafsheh, A., Limberopoulos, N.I., Derov, J.S., Walker, D.E. and Astratov, V.N. (2014). Advantages of microsphere-assisted super-resolution imaging technique over solid immersion lens and confocal microscopies. *Applied Physics Letters*, 104(6), p.061117. doi:<https://doi.org/10.1063/1.4864760>.

17. Fornasiero, E.F. and Rizzoli, S.O. (2014). Super-resolution Microscopy Techniques in the Neurosciences.
18. Weissart, K., Fuchs, J. and Schubert, V. (2016). Structured Illumination Microscopy (SIM) and Photoactivated Localization Microscopy (PALM) to Analyze the Abundance and Distribution of RNA Polymerase II Molecules on Flow-sorted Arabidopsis Nuclei. *BIO-PROTOCOL*, 6(3). doi:<https://doi.org/10.21769/bioprotoc.1725>.
19. Delcanale, P., Miret-Ontiveros, B., Arista-Romero, M., Pujals, S. and Albertazzi, L. (2018). Nanoscale Mapping Functional Sites on Nanoparticles by Points Accumulation for Imaging in Nanoscale Topography (PAINT). *ACS nano*, [online] 12(8), pp.7629–7637. doi:<https://doi.org/10.1021/acsnano.7b09063>.
20. Eberle JP, Rapp A, Krufczik M, Eryilmaz M, Gunkel M, Erfle H, et al. Super-Resolution Microscopy Techniques and Their Potential for Applications in Radiation Biophysics. New York: Humana Press, New York, NY; 2017. [https://link.springer.com/protocol/10.1007/978-1-4939-7265-4\\_1](https://link.springer.com/protocol/10.1007/978-1-4939-7265-4_1)
21. Haupt, R. L., & Haupt, S. E. (1998). Practical genetic algorithms. John Wiley & Sons.
22. Parmar, A., Katariya, R., & Patel, N. (2018). A review on random forest: An ensemble classifier. *International Journal of Computer Applications*, 182(11), 10–15.
23. Patil, R., & Chopade, N. (2015). Noise reduction using wavelet transform and singular vector decomposition. *International Journal of Engineering Trends and Technology*, 23(7), 332–336.
24. Vonesch, C., & Unser, M. (2006). A fast thresholded Landweber algorithm for wavelet-regularized multidimensional deconvolution. *IEEE Transactions on Image Processing*, 15(1), 346–357. <https://doi.org/10.1109/TIP.2005.860363>
25. Montero, R. S., & Bribiesca, E. (2009). State of the art of compactness and circularity measures. *International Mathematical Forum*, 4(25), 1305–1335.
26. Fogel, D. B. (2000). *Evolutionary computation: Toward a new philosophy of machine intelligence* (2nd ed.). Wiley-IEEE Press.
27. de Liedekerke Beaufort, G. (2024). Development of a fast, three-dimensional particle localisation and tracking method for live-cell microscopy (MPhil thesis). Imperial College London.
28. Donoho, D.L. and Johnstone, I.M. (1994). Ideal spatial adaptation by wavelet shrinkage. *Biometrika*, 81(3), pp.425–455. <https://doi.org/10.1093/biomet/81.3.425>
29. Gonzalez, R.C. and Woods, R.E. (2018). *Digital image processing* (4th ed.). Pearson.
30. Meireles S. Transport of macromolecules across endothelium and its relevance to atherosclerosis [Master's thesis]. London: Imperial College London; 2022.
31. Ross R. Atherosclerosis—an inflammatory disease. *N Engl J Med*. 1999;340(2):115–26.
32. Weinberg PD, Ethier CR. Twenty-fold difference in transendothelial macromolecular permeability between aortic regions of rabbit is associated with size-selective transport. *J Physiol*. 2007;582(Pt 2):903–20.
33. Davies MG, Hagen PO. Pathobiology of intimal hyperplasia. *Br J Surg*. 1994;81(9):1254–69.
34. Ziegler T, Alexander Y, Khawaja A, et al. Venous graft disease: pathogenesis and strategies for prevention. *Arterioscler Thromb Vasc Biol*. 2019;39(5):e48–e56.

35. Thijssen DHJ, Carter HH, Green DJ. Arterial structure and function in vascular grafts. *Nat Rev Cardiol.* 2015;12(12):701–12.
36. Chi JT, Chang HY, Haraldsen G, et al. Endothelial cell diversity revealed by global expression profiling. *Proc Natl Acad Sci USA.* 2003;100(19):10623–8.
37. Rembotte L. Transport of Macromolecules Across the Arterial Endothelium and its Relevance to Atherosclerosis [undergraduate thesis]. Imperial College London; 2022.
38. Diaspro A, editor. *Confocal and Two-Photon Microscopy: Foundations, Applications, and Advances.* Wiley-Liss; 2001.
39. Pawley JB. *Handbook of Biological Confocal Microscopy.* 3rd ed. Springer; 2006.
40. Frank M. Sacks, Hannia Campos, Low-Density Lipoprotein Size and Cardiovascular Disease: A Reappraisal, *The Journal of Clinical Endocrinology & Metabolism*, Volume 88, Issue 10, 1 October 2003, Pages 4525–4532, <https://doi.org/10.1210/jc.2003-030636>
41. Ye, M. and Searson, P.C. (2011). Blinking in quantum dots: The origin of the grey state and power law statistics. *Physical Review B*, 84(12). doi:<https://doi.org/10.1103/physrevb.84.125317>.

## **8 Appendix**

### **Appendix A – Project Management Assessment & Lessons learned**

Our initial plan proposed early background research and lab training (starting in January) to build key skills for cell culturing and fluorescent labelling, followed by confocal imaging. In practise, this early lab start worked well, we completed the relevant induction on schedule, providing essential familiarity with cell handling and imaging techniques.

However, near the project's end, unexpected challenges arose. Our lab supervisor, Dr Bolanle became heavily engaged with another research project, limiting availability for guidance. Additionally, Quantum Dots produced inconsistent results, prompting us to experiment with different wells and fluorescent markers (FITC-avidin) – a pivot that demanded extra lab time and support. On the software side, unspecified MATLAB versions introduced compatibility problems, and the inherited code lacked robust error handling, causing significant errors and delays. This diverted attention away from planned algorithm training and optimisation as we struggled to debug and stabilise the code.

Overall, our project management cantered on adapting workflow and timeline to unanticipated imaging failures, supervisory constraints and coding obstacles. Despite these setbacks, our early wet-lab start has paid-off by giving us room to handle unforeseen problems. Ultimately, these experiences underscore the importance of contingency planning and thorough software validation, ensuring progress despite unexpected challenges.

#### **Lesson 1: Effective Time Management and Contingency Planning**

Although we scheduled cell culturing and fluorescence labelling tasks weekly and arranged microscope filming sessions accordingly within the same or following week, overall, we underestimated the total time required to fully validate all aspects of our microscopy approach. Throughout the project, unforeseen operational mistakes occurred, causing delays and incomplete data collection. Particularly towards the project's final stages, confocal microscope slots were fully booked, making additional imaging impossible within the available timeframe. This experience underscores the importance of comprehensive contingency planning. Future project plans should include sufficient buffer periods to account for unexpected issues, increased demand for shared resources, and potential operational errors, thereby ensuring thorough data acquisition and project objectives are met without undue pressure.

#### **Lesson 2: Clear Role Definition and Balanced Task Allocation**

Our project lacked clearly defined roles and responsibilities in the lab sessions, leading team members to undertake tasks based on individual availability. Consequently, awareness of overall progress and specific experimental details became fragmented among team members, significantly increasing communication overhead and inefficiency during report writing. Moreover, the critical task of developing and debugging the project code was predominantly managed by only a few members. This uneven workload distribution resulted in increased pressure on those individuals and limited opportunities for effective support from the rest of the team. Clearly defined roles and more balanced task allocation from the outset would ensure equitable workload distribution, enhance

information continuity, reduce individual stress, and improve overall project efficiency and communication.

### **Lesson 3: Importance of Early Theoretical Preparation**

Early in the project, we devoted significant time to acquiring theoretical knowledge by extensively reviewing relevant literature. This proactive approach greatly facilitated the subsequent experimental design, data interpretation, and report writing stages. Our solid theoretical foundation allowed us to quickly address experimental uncertainties, understand methodological contexts, and articulate our findings clearly in the final report. Moving forward, it is crucial to maintain this habit of thorough initial literature research and theoretical groundwork.

## **Appendix B - Wet Lab Methods**

### **Coating Culture dishes with Biotinylated Gelatin**

#### **1. Gelatin Preparation and Dissolution:**

Gelatin from porcine skin (G 2500) was dissolved in 0.1 mol/L sodium bicarbonate buffer (pH 8.3) at a final concentration of 10 mg/mL. To ensure complete dissolution, the gelatin mixture was heated to approximately 70 °C in a water bath with constant stirring. This process typically took around 30 minutes, after which the solution was clarified by low-speed centrifugation (10 000 × g, 5 minutes, room temperature) to remove any remaining particulates. The clarified solution was then transferred back to a clean beaker under continuous stirring.

#### **2. Biotinylation of Gelatin:**

Separately, EZ-Link NHS-LC-LC-Biotin was dissolved in DMSO at 5.7 mg/mL. A portion of this DMSO–biotin solution was added to the warmed gelatin solution such that the final biotin concentration in the combined mixture reached approximately 0.57 mg/mL (e.g., 5 mg of biotin in 888 µL DMSO added to 10 mL gelatin solution). This mixture was stirred continuously at room temperature for about 1 hour to allow the biotin to conjugate with the gelatin.

#### **3. Dilution and Sterilization**

After conjugation, the biotinylated gelatin was further diluted with additional 0.1 mol/L bicarbonate buffer (pH 8.3) to achieve the desired final biotin concentration (for instance, from 0.57 mg/mL down to ~0.25 mg/mL). The resulting solution was then sterile filtered sequentially through 0.45 µm and 0.22 µm filters to remove any microbial contaminants or residual particulates.

#### **4. Coating Culture Dishes**

For 35 mm culture dishes, 2 mL of the sterile-filtered biotinylated gelatin solution was dispensed into each dish (adjust volumes as needed for your plate or dish format). The dishes were sealed with sterilized parafilm and placed at 4 °C overnight to allow thorough adsorption of the gel. Finally, any excess gelatin solution was removed, and the dishes were left to warm to room temperature before introducing cells or fluorescent markers (e.g., TetraSpeck microspheres or Quantum Dots).

### **Quantum Dot (QD) Preparation**

Quantum Dot 800 (Thermo Fisher Scientific, 1 µM stock) was placed *undiluted* into a filtration device (**use a molecular-weight-cutoff or pore-size filter appropriate for nanoparticles**) that

had been **pretreated with albumin** to reduce QD adherence to the membrane. Initially, 1.5 mL of PBS were added, and the assembly was ultracentrifuged at 10,000 rpm for 15 minutes to remove unbound or excess material. The supernatant was discarded, and another 1.5 mL of PBS was added; the sample was then centrifuged for 10 minutes. This 10-minute spin was repeated two additional times—each time discarding the supernatant and adding 1.5 mL of PBS.

After these washes, the filter assembly contained mostly QDs. To retrieve them at a final concentration of 76 nM in an 800 µL solution, **740 µL of growth medium** were added directly into the filter. The medium, now containing the resuspended QDs, was collected from the filter device, ensuring minimal loss of nanoparticles. This QD solution was then ready for subsequent cell culture or imaging steps.

In addition, lower concentration working solutions were prepared from a separate **7.6 nM** QD stock (made by mixing **6.08 µL** of the original QD stock with **794 µL** of growth medium). For a **0.78 nM** solution, **80 µL** of the 7.6 nM QD suspension were withdrawn and mixed with **720 µL** of growth medium. To achieve **0.078 nM**, **8 µL** of the 7.6 nM stock were combined with **794 µL** of growth medium. All QD solutions were prepared immediately before use to minimise aggregation and ensure consistent fluorescence.

### **TetraSpeck™ Dilutions**

The stock solution of TetraSpeck™ microspheres had an initial concentration of  $1.4 \times 10^{13}$  particles/mL. To align with the QD dilutions, working solutions were prepared at **0.76 nM**, **0.38 nM**, and **0.076 nM**. For 0.76 nM, **26.43 µL** of the stock were withdrawn; for 0.38 nM, **13.215 µL**; and for 0.076 nM, **2.643 µL**. In each case, growth medium was added until the final volume reached 800 µL. This ensured microsphere concentrations comparable to the QD levels used in our imaging experiments.

### **Transfer and seeding of HAECs**

First, the T75 flask containing HAECs is gently rinsed twice with 5 mL of PBS to remove any residual medium and non-adherent cells. Next, 2 mL of trypsin are added to detach the cells, which typically requires 3–4 minutes at room temperature. Gentle tapping of the flask helps dislodge any residual adherent cells, and microscope inspection confirms complete detachment.

Subsequently, 10 mL of growth medium are introduced to neutralise and dilute the trypsin, preventing excessive proteolytic activity. The entire cell-trypsin-medium mixture is transferred to a conical tube and centrifuged at 1,500 rpm for 10 minutes. After discarding the supernatant, the remaining cell pellet is resuspended in 10 mL of fresh growth medium, yielding a final suspension that typically contains up to 5 million cells. Cells can then be seeded into individual wells at the desired density, ensuring uniform distribution and facilitating further imaging or experimental procedures.

### **Cell Fixation Protocol**

Once the wells have been coated, HAECs seeded, and fluorescent probes (Qdots or FITC-avidin) introduced, cell fixation is performed as follows. First, **2 mL of 4% paraformaldehyde (PFA)** solution are added directly to each well, ensuring complete coverage of the cell layer. The plate is then incubated for **15 minutes at room temperature**, allowing the PFA to crosslink cellular components. After incubation, the PFA solution is carefully removed and the wells are gently **rinsed with PBS** to remove residual fixative. This step concludes fixation; DRAQ5 staining (if required) can be added afterward.

### **Nuclear Staining with DRAQ5**

For nuclear labelling, DRAQ5 (Thermo Fisher Scientific) was diluted at 1:1000 in standard growth medium, and **0.5 mL** of this solution was added to each well. The plate was then incubated at 37 °C for 5 minutes, allowing sufficient uptake for clear nuclear fluorescence during subsequent imaging.



**Three types of culture wells were used:** [standard plastic bottom wells (Corning 3512)], [glass-bottomed (1.5H) 35 mm dishes (Ibidi 81158)], and [polymer-bottomed (#1.5) 35 mm dishes (Ibidi 81156)].

# Appendix C - Parameter Definitions

## Some Definitions

- $C = [\sum_{n=1}^N I_n * x_n / \sum_{n=1}^N I_n, \sum_{n=1}^N I_n * y_n / \sum_{n=1}^N I_n]$ 
  - $\Rightarrow$  Centre of Gravity of PSF
  - $I_n$  is pixel intensity at pixel  $n$  with coordinate  $x_n, y_n$
  - $N$  is the total number of Pixels determined to be part of the PSF
- $I_{dev}(x, y) = I(x, y) - I_{gauss}(x, y) \Rightarrow$  Deviation from Gaussian
  - $I_{gauss}$  is the expected intensity at pixel  $n$  according to the gaussian approximation
- $C_{gauss} = \left[ \frac{\sum_{n=1}^N I_n * I_{gauss,n} * x_n}{\sum_{n=1}^N I_n * I_{gauss,n}}, \frac{\sum_{n=1}^N I_n * I_{gauss,n} * y_n}{\sum_{n=1}^N I_n * I_{gauss,n}} \right]$ 
  - PSF Centre using a Gaussian Mask Method
  - $N$  is the total number of Pixels determined to be part of the PSF
- $\hat{x} = (x - C_x)$  or  $\hat{x}_{gauss} = (x - C_{gauss,x}) \Rightarrow$  distance from estimated PSF centre (weighted vs gaussian)
- $\hat{X}_{gauss-I} = \begin{pmatrix} \hat{x}_{gauss,1} \\ \vdots \\ \hat{x}_{gauss,M} \end{pmatrix}$  or  $\hat{X}_{gauss-dev} = \begin{pmatrix} \hat{x}_{gauss,1} \\ \vdots \\ \hat{x}_{gauss,P} \end{pmatrix}$  where  $M = \sum_{n=1}^N I_n$  and  $P = \sum_{n=1}^N I_{dev,n}$ 
  - $\Rightarrow$  Vector of  $x$  distances where each pixel gets a number of entries equal to its intensity or deviation in expected intensity

$n = 3$ $I_3$ (1,2)	$n = 4$ $I_4$ (2,2)
$n = 1$ $I_1$ (1,1)	$n = 2$ $I_2$ (2,1)

## Some More Definitions

- $\sigma_x = \sqrt{\sum_{n=1}^N \hat{x}_n^2 * I_n / \sum_{n=1}^N I_n} \Rightarrow$  Definition of std
- $E(\hat{x}) = \frac{1}{N} * \sum_{n=1}^N \hat{x}_n \Rightarrow$  Definition of the arithmetic mean function
- $Inv(i, j) = \sum_{n=1}^N \hat{x}_n^i * \hat{y}_n^j * I_n^{norm} / \sum_{n=1}^N (I_n^{norm})^{1+(i+j)/2} \Rightarrow$  Normalized Spatial Moment
  - $I_n^{norm}$  is  $I_n$  expected it has been normalized to be in the range of (0,1):  $I_n^{norm} = \frac{I_n - I_{min}}{I_{max} - I_{min}}$
- $Q_{nth, I-x} =$  nth quantile of the  $I \sim x$  distribution where  $I$  acts as the pdf over  $x$
- $\theta_{n,1} =$  angle of pixels with respects to PSF centre, restricted to  $0^\circ$ - $180^\circ$  (measure of direction of major axis)
- $\theta_{n,2} =$  angle of pixels with respects to PSF centre,  $0^\circ$  - $360^\circ$  (measure of distortion)

## I-X Metrics (Intensity Distribution over X) & $I_{dev}$ -X Metrics

1.  $M_1 = \frac{2}{(y_{max} - y_{min}) + (x_{max} - x_{min})} * \frac{\sum_{n=1}^N \hat{x}_n^2 * I_{dev,n}}{\sum_{n=1}^N I_{dev,n}}$ 
  - Normalised variance of  $I_{dev}$  along the  $x$  axis about centre of gravity;  $x_{max}$  and  $x_{min}$  are the minimum and maximum  $x$  coordinate in the PSF respectively
2.  $M_2 = \frac{1}{\sigma_{gauss,x}^2} (Q_{0.75, I \sim x} - Q_{0.25, I \sim x})$ 
  - IQR/STD of X-I distribution; where  $Q_n$  is the nth quartile of the I-X distribution and  $\sigma_{gauss,x}$  is the std of the elliptical gauss PSF model in the  $x$  direction
3.  $M_3 = K(\hat{x}_{gauss}, I_{dev})$ 
  - Where  $K$  is the kurtosis function;  $M_3$  is the Kurtosis of the distribution of  $I_{dev}$  on the normalized  $x$  domain (normalized by the gauss estimated centroid of the PSF)

## I-Y Metrics (Intensity Distribution over Y) & $I_{dev}$ -Y Metrics

1.  $M_4 = \frac{2}{(y_{max}-y_{min})+(x_{max}-x_{min})} * \frac{\sum_{n=1}^N \hat{y}_n^2 * I_{dev,n}}{\sum_{n=1}^N I_{dev,n}}$ 
  - Normalised variance of  $I_{dev}$  along the y axis about centre of gravity
2.  $M_5 = \frac{1}{\sigma_{gauss,y}^2} (Q_{0.75,I \sim y} - Q_{0.25,I \sim y})$ 
  - IQR/variance of X-I distribution; where  $Q_n$  is the nth quartile of the I-Y distribution and  $\sigma_{gauss,x}$  is the std of the elliptical gauss PSF model in the x direction
3.  $M_6 = K(\hat{y}_{gauss}, I_{dev})$ 
  - Where  $K$  is the kurtosis function;  $M_6$  is the Kurtosis of the distribution of  $I_{dev}$  on the normalized x domain (normalized by the gauss estimated centroid of the PSF)

## I Metrics (Properties of the PSF Intensity) & $I_{dev}$

1.  $M_7 = (I_{max}-I_{min})/\sigma_I$ 
  - Ratio of the intensity range to the std of the intensity
2.  $M_8 = Corr(I, I_{gauss})$ 
  - Where  $Corr()$  is a correlation function calculating the Pearson Correlation Coefficient between  $I$  and  $I_{gauss}$
  - $M_8$  is the correlation between the pixel intensities and their corresponding estimated from the gaussian PSF model (different way of looking at deviation from the gaussian model other than magnitude difference)
3.  $M_9 = Med(|I - Med(I)|)$ 
  - Where  $Med()$  is the median function returning the median of the input;
  - $M_9$  is the MAD of  $I$ ; Median absolute deviation which is the median of the absolute deviations from the data's median
  - It is considered a very robust measure of variability
4.  $M_{10} = \sum_{n=1}^N |I_n - Med(I)| / \sum_{n=1}^N I_n$ 
  - Mean absolute deviation of  $I$
5.  $M_{11} = \sum_{n=1}^N |I_{dev,n} - Med(I_{dev})| / \sum_{n=1}^N I_{dev,n}$ 
  - Mean absolute deviation of  $I_{dev}$

## I-X-Y Metrics & $I_{dev}$ -X-Y Metrics

1.  $M_{12} = \frac{1}{2} * \left\{ \frac{(Q_{0.75,I_{dev}-\hat{x}_{gauss}} - Q_{0.25,I_{dev}-\hat{x}_{gauss}})}{\max(\hat{x}_{gauss})} + \frac{(Q_{0.75,I_{dev}-\hat{y}_{gauss}} - Q_{0.25,I_{dev}-\hat{y}_{gauss}})}{\max(\hat{y}_{gauss})} \right\}$ 
  - Mean of the IQR of the deviation distribution in x and y normalized by the maximum x and y coordinate
2.  $M_{13} = \frac{1}{E(\hat{x}_{gauss}^2 + \hat{y}_{gauss}^2)} \sqrt{(Med(|\hat{x}_{gauss}-I - Med(\hat{x}_{gauss}-I)|))^2 + (Med(|\hat{y}_{gauss}-I - Med(\hat{y}_{gauss}-I)|))^2}$ 
  - MAD of the Euler distance from gauss estimated PSF centroid
3.  $M_{14} = \frac{1}{E(\hat{x}_{gauss}^2 + \hat{y}_{gauss}^2)} \sqrt{(E(|\hat{x}_{gauss}-dev - Med(\hat{x}_{gauss}-dev)|))^2 + (E(|\hat{y}_{gauss}-dev - Med(\hat{y}_{gauss}-dev)|))^2}$ 
  - MAD of the Euler distance from gauss estimated PSF centroid based on the deviation distribution. Normalised by the mean Euler distance
4.  $M_{15} = \frac{(y_{max}-y_{min})+(x_{max}-x_{min})}{2 * E(\hat{x}_{gauss}^2 + \hat{y}_{gauss}^2)}$ 
  - Ratio of the mean of the x/y range to the mean Euler distance
5.  $M_{16} = \frac{(y_{max}-y_{min})+(x_{max}-x_{min})}{(\sigma_{gauss,y} + \sigma_{gauss,x})}$ 
  - Ratio of the mean of the x/y range to the mean gaussian std in x/y
6.  $M_{17} = \sigma_{gauss,x} / \sigma_{gauss,y}$ 
  - Elliptical ratio of the elliptical gauss PSF model; ratio of the estimated normal std in x and the normal std in y

## Moment Invariants & Centre Deviation

$$1. M_{18} = Inv(2,0) + Inv(0,2)$$

- Zunic Circularity Descriptor – Zunic et. al 2010

$$2. M_{19} = (Inv(2,0) - Inv(0,2))^2 + 4 * Inv(1,1)^2$$

- Moment Invariant of the Second Kind (Hu et al 1962)

$$3. M_{20} = (Inv(3,0) - 3 * Inv(1,2))^2 + (3 * Inv(2,1) - Inv(0,3))^2$$

- Moment Invariant of the Third Kind (Hu et al 1962)

$$4. M_{21} = (Inv(3,0) + Inv(1,2))^2 + (Inv(2,1) + Inv(0,3))^2$$

- Moment Invariant of the Fourth Kind (Hu et al 1962)

$$5. M_{22} = \sqrt{(E(x) - C_{gauss,x})^2 + (E(y) - C_{gauss,y})^2}$$

- Euler distance between the gaussian estimated PSF centre and simple averaging of pixel positions; measure of deviation of the centre from the PSF geometric centre

## SQRT(X^2+Y^2)-I Metrics

$$1. M_{23} = \frac{\sum_{n=1}^N \sqrt{\hat{x}_{gauss,n}^2 + \hat{y}_{gauss,n}^2} * I_n}{E(I) * \sum_{n=1}^N I_n}$$

- STD of Euler distance from gaussian centre normalized by mean pixel intensity

$$2. M_{24} = Med(\sqrt{\hat{X}_{gauss-I}^2 + \hat{Y}_{gauss-I}^2})$$

- Median Euler distance from gaussian estimated centre weighted by I

$$3. M_{25} = Skw(\sqrt{\hat{X}_{gauss-I}^2 + \hat{Y}_{gauss-I}^2})$$

- Where Skw() is the skew of the Euler distance from the gaussian Centroid with I as pdf (weighting)

$$4. M_{26} = Corr(I, \sqrt{\hat{x}_{gauss}^2 + \hat{y}_{gauss}^2})$$

- Pearson correlation coefficient between the pixel intensity and the Euler distance from the gaussian estimated centroid

$$5. M_{27} = E(\sqrt{\hat{X}_{gauss-I}^2 + \hat{Y}_{gauss-I}^2} - E(\sqrt{\hat{X}_{gauss-gauss}^2 + \hat{Y}_{gauss-gauss}^2}))$$

- Mean deviation from the expected mean Euler distance from gaussian estimated centre

$$6. M_{28} = Corr(I_{dev}, \sqrt{\hat{x}_{gauss}^2 + \hat{y}_{gauss}^2})$$

- Pearson correlation coefficient between the pixel intensity deviation and the Euler distance from the gaussian estimated centroid

## Angle Metrics

$$1. M_{29} = K(\theta_1)$$

- Skew of the  $\theta_1$ -I distribution; the  $\theta_1$  of each pixel is weighted by the pixel Intensity =>  $\theta_1$

$$2. M_{30} = atan2(\sum_{i=1}^M \sin(\theta_{i,1}), \sum_{i=1}^M \cos(\theta_{i,1}))$$

- Angular mean of the  $\theta_1$ -I distribution; Kanti et al. 1999

$$3. M_{31} = Mode(\theta_2)$$

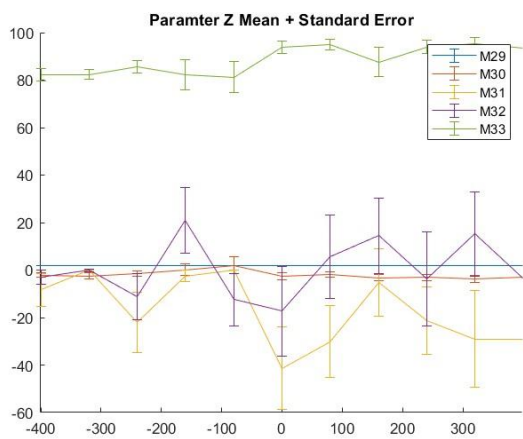
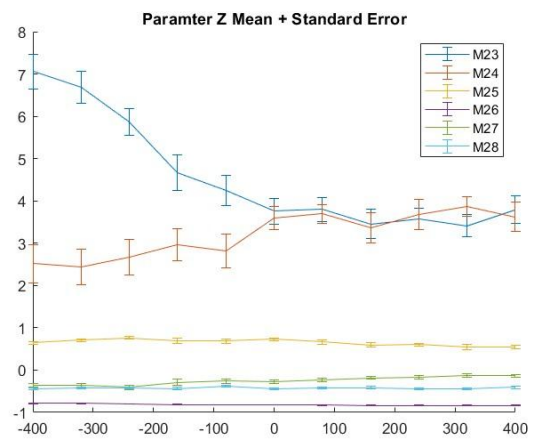
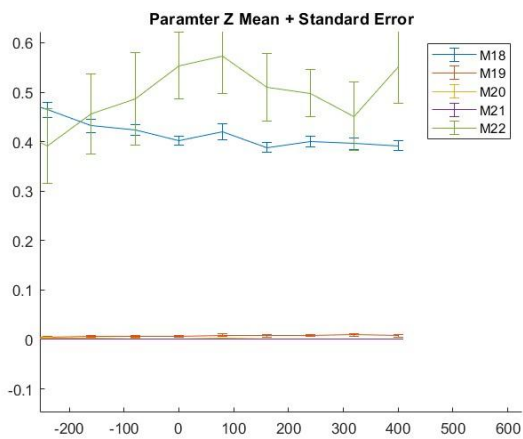
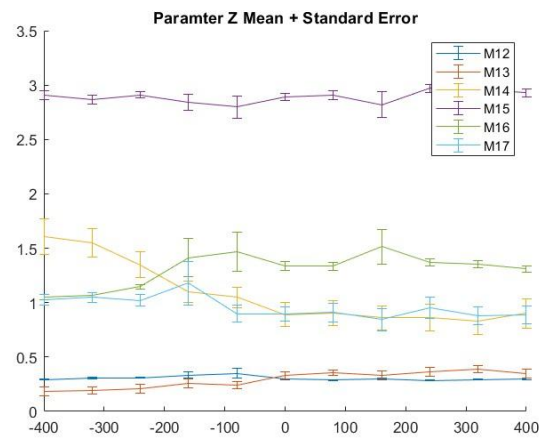
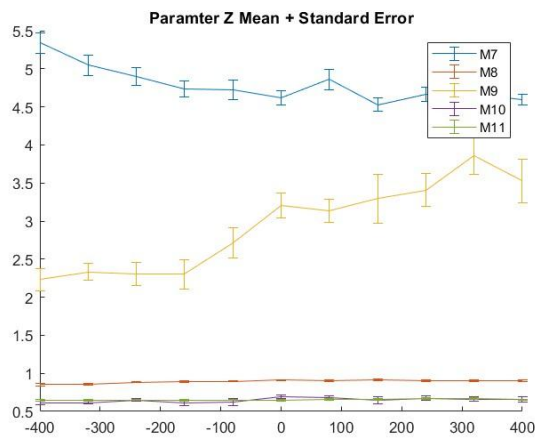
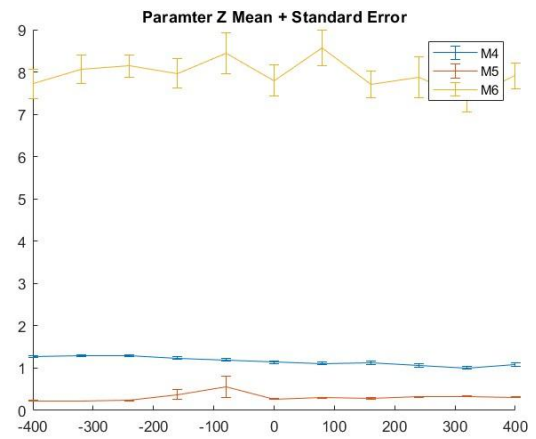
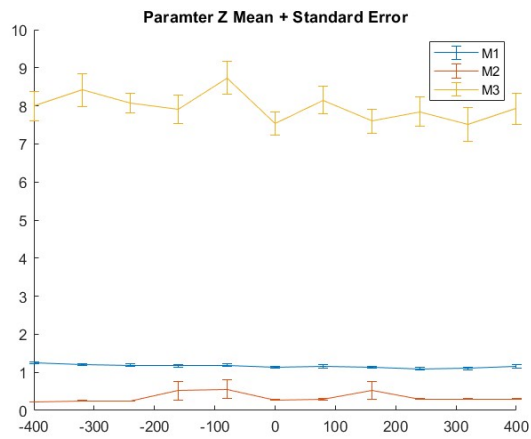
- Mode of the  $\theta_2$ -I distribution

$$4. M_{32} = atan2(\sum_{i=1}^M \sin(\theta_{i,2}), \sum_{i=1}^M \cos(\theta_{i,2}))$$

- Angular mean of the  $\theta_2$ -I distribution; Kanti et al. 1999

$$5. M_{33} = \sigma_{\theta_2}$$

- STD of the  $\theta_2$ -I distribution



## Appendix D - Code of Adaptive Wavelet Filter

```
function denoised = wavelet_denoise_adaptive(array, lambda)

% Step 1: Remove background
if lambda == 0
    Imean = mean(array(:));
else
    Imean = lambda;
end
img_shifted = array - Imean;

% Step 2: Wavelet decomposition
level = 2;
wname = 'sym4';
[C, S] = wavedec2(img_shifted, level, wname);

% Step 3: Universal soft-threshold
T = median(abs(C(:))) / 0.6745 * sqrt(2 * log(numel(array))); % Universal threshold
C_thresh = sign(C) .* max(abs(C) - T, 0); % soft thresholding

% Step 4: Reconstruction
denoised = waverec2(C_thresh, S, wname);

% Step 5: Restore and suppress low background
bg_sigma = std(array(:));
adaptive_thresh = Imean + 0.5 * bg_sigma;
denoised(denoised < adaptive_thresh) = 0;
end
```